

Sediment transport over an accretional intertidal flat with influences of reclamation, Jiangsu coast, China

Ya Ping Wang^{a,*}, Shu Gao^a, Jianjun Jia^b, Charlotte E.L. Thompson^c, Jianhua Gao^a, Yang Yang^a

^a Ministry of Education Key Laboratory for Coast and Island Development, Nanjing University, Nanjing 210093, China

^b Key Laboratory of Submarine Geo-Sciences, Second Institute of Oceanography, State Oceanic Administration, Hangzhou 310012, China

^c School of Ocean and Earth Science, University of Southampton, Southampton SO14 3ZH, UK

ARTICLE INFO

Article history:

Received 14 June 2010

Received in revised form 7 January 2011

Accepted 17 January 2011

Available online 26 January 2011

Keywords:

current-wave interactions
suspended sediment concentrations
intertidal flats
reclamation
Jiangsu coast

ABSTRACT

This paper focuses on the hydrodynamic and suspended sediment transport processes in response to sequential reclamations over the intertidal flat, Jiangsu coast, which used to be one of the widest intertidal flats in China. Investigations into the sediment transport patterns reveal that net suspended sediment fluxes increased from 10^2 kg m^{-1} on the upper intertidal flat to $10^{3-4} \text{ kg m}^{-1}$ on the lower intertidal flat, per tidal cycle. This variation was caused mainly by the phases of the current velocity, suspended sediment concentration (SSC), local bed geomorphology, inundation patterns, and extreme weather conditions. The longshore component of tidal currents intensifies seaward over the intertidal flat. Extreme weather conditions (e.g. storms) and strong winds were important factors affecting the current velocity structures, the intensity of residual currents, and the SSCs. The SSCs were characterized by several peaks throughout the tidal cycle. These peaks were associated with strong currents, combined wave-current interactions and intense turbulences due to the initial flood surge. Furthermore, the suspended sediment was finer and contained more clay materials during the flood phase of the tidal cycle, than during the ebb. Fine particles were transported within the upper water column by landward residual currents, but coarse particles were transported within the lower water column by seaward residual currents. Overall, residual currents were apt to transport fine-grained sediment landward and coarse-grained sediment seaward. This pattern indicates that the suspended sediment fluxes are highly variable in the water column, even for very shallow tidal environments. The cross-shore component accounted only for a small percentage of the total sediment flux. However, this part of sediment supply dominated accretion over the intertidal flat.

The intertidal flat has become narrower and steeper, following sequential reclamations. A negative feedback process existed to maintain the convex profile shape, although the human activities (i.e. reclamation) could have modified the natural process. The surficial sediment tended to become finer on the mid-upper intertidal flat but coarser on the lower intertidal flat following reclamations, in response to a reduction in the tidal currents over the intertidal zone and enhancement of wave action over the lower intertidal flat. Accretion, with high rates, was maintained by landward transport of sediment. In such an accretional system with influences of reclamation, the width or slope of the intertidal flat is adjusted continuously. Before the cease of reclamation, the intertidal flat is unable to achieve an equilibrium shape.

© 2011 Elsevier B.V. All rights reserved.

1. Introduction

Intertidal flats are areas of significant land–ocean interaction; they are important coastal geomorphological systems which provide habitats for wild life, resources for land reclamation and protection for the coast against extreme storm events (Allen and Pye, 1992; Wang et al., 1999; Allen, 2000). In addition, intertidal flats represent a sink for organic carbon and play an important role in global carbon cycling and climate change (Kremer et al., 2005). In particular accreting intertidal flat, being

a sediment sink, plays an important role in coastal defense (Kirby, 2000). Thus, the physical processes of accretion, erosion and reworking on intertidal flats are immensely important for coastal planning, engineering, and ecosystem maintenance.

Previous studies have shown that the processes controlling the evolution of intertidal flats are highly complex, controlled by multidirectional non-steady tidal currents, waves and rainfall (Green and Coco, 2007), and linked to large-scale patterns of sediment texture (Ryan and Cooper, 1998), biogeochemical and zoobenthos effects (Widdows et al., 2000; Zhou et al., 2008) and halophytic plant cover (Yang and Chen, 1995; French et al., 2000; Yang et al., 2003; Gao, 2009b). Storms may cause erosion of the bed and sediment movement towards offshore waters (Le Hir et al., 2000), but net accumulation on salt marshes (on the

* Corresponding author. Tel.: +86 25 83686010; fax: +86 25 83595387.

E-mail address: ypwang@nju.edu.cn (Y.P. Wang).

upper part of the intertidal flat): local wind waves generally cause erosion by seaward transport over low areas of the flat and net deposition onshore over high areas (de Haas and Eisma, 1993; Christie et al., 1999). Sediment fluxes over the intertidal flat have also been found to be affected by time-varying velocity asymmetry (Roberts et al., 2000) and settling lag effects (Pritchard and Hogg, 2003). In addition, sediment supply is an important component of the long-term sediment budget (Andersen et al., 2006). The sediment transport patterns over the intertidal flat can be described in terms of suspended load and bedload transport, with the transport rate varying at different temporal and spatial scales (Quaresma et al., 2007). However, these processes are poorly understood in comparison with those on sandy beaches (Dyer, 2000), because intertidal flats are a difficult environment for field work: logistic and safety constraints often become an obstacle for *in situ* measurements and sampling. Since accurate *in situ* measurements of current velocity structures are required for the calculation of bottom boundary layer parameters (Collins et al., 1998; Wang et al., 2004), it is essential to develop an efficient measuring technique to collect high-resolution data autonomously, at a range of spatial and temporal scales (Wang et al., 2006).

Reductions in intertidal flat width, caused by reclamation with artificial embankments, have been a prominent feature of the southwestern coasts of the Yellow Sea (Jiangsu coasts) for the past few decades. Over the last few centuries, the intertidal flat of the central Jiangsu coast has represented a typical accretional system; it received sediments from both the Changjiang (Yangtze) River and the Yellow River (during 1128–1855). In the past, only limited hydrodynamic measurements were carried out using analogue, impeller-type current meters on the Jiangsu intertidal flats. The data sets obtained were therefore generally of low quality in terms of vertical and temporal resolution (Yang, 1982; Ren, 1986; Zhang, 1992; Wang et al., 1999). Higher resolution, *in situ* measurements were needed to provide detailed data sets, with enhanced horizontal (along the cross-section) and vertical (within the water column) resolutions, to study the hydrodynamic and sediment dynamic processes of the intertidal flats. On the other hand, reclaimed intertidal flats in Europe are increasingly being abandoned, mainly for the purposes of wetlands restoration and coastal protection, which have been studied recently (French et al., 2000; Mai and Bartholomä, 2000; Symonds and Collins, 2007). In China, however, the coasts have been undergoing increasing reclamation since 1950. The reclaimed areas were mainly limited to the supratidal zone before 1978 (JCC, 1995; Chung et al., 2004). The intertidal areas have been reclaimed broadly since 1978, which has resulted in a decrease of the tidal prism and reduction of the intertidal flats. These reclamations have also significantly changed the sedimentary preservation, which should be taken into account in the calculation of preservation potential (Gao, 2009a). In addition, the dams constructed on rivers (e.g. the Three Gorges Dam, on the Changjiang River) have trapped abundant sediments, such that sediment fluxes to the sea and the supply to intertidal flats are decreasing. The effects of this reduction in sediment supply on the sediment dynamics and geomorphology of the tidal flats are still not clear. In this contribution, we investigate the hydrodynamics (e.g. tidal currents and wind waves), suspended sediment fluxes and bed changes over an accretional intertidal flat, using high-resolution instruments (including ADCP, MIDAS400, ADV and turbidity meters). The data obtained were used to analyze the vertical distributions of hydrodynamics (current velocity and residual components) and associated suspended sediment properties (SSC and grain size). The response of intertidal flats to the continuous reclamation activities is also examined.

2. The study area

The study area is located on the Jiangsu coast, China, which is situated between the Changjiang (Yangtze) River estuary and the

abandoned Yellow River mouth (Fig. 1A). Fine-grained sediments of the intertidal flats were from Yellow River, which entered the southern Yellow Sea between 1128 AD and 1855 AD. The adjacent waters are characterized by a large radial-shaped tidal ridge (or linear sandbank) system in the southwestern Yellow Sea, with the sandbanks converging at Jianggang. These sandbanks diverge to a depth of 20–30 m and the sand ridge field is approximately 90 km in width in an east–west direction and 200 km in length from the northwest to the southeast (Liu et al., 1989; Wang, 2002). The intertidal flats here are sheltered partially by the radial tidal ridge system, similar to the sheltered intertidal flat at Calais, Northern France and intertidal flats in some semi-enclosed embayments (Lee, et al., 2004; Hequette and Aernouts, 2010).

The intertidal flat is located in a macro-tidal area, with an average tidal range of 3.9–5.5 m, and a regularly semi-diurnal tide (Ren, 1986). Two tidal wave systems, i.e. the East China Sea progressive tidal wave and the Southern Yellow Sea rotary tidal wave, converge near the coastal waters of Jianggang (Zhang, 1992). Under such hydrodynamic conditions, the mean tidal range reaches 5 m in the Jianggang area, decreasing southward and northward. In general, the flood dominates over the ebb and has a significant influence on the patterns of net sediment transport; consequently, fine-grained sediments are transported landward and accumulate over the intertidal flat (Zhang, 1992). Moreover, abundant sediment supply is derived from the radial tidal ridge system off the Jiangsu coast, the Changjiang River and the abandoned Yellow River delta (Ren, 1986; Zhang, 1992). Thus, most of the Jiangsu coast is characterized by continuous growth of intertidal mudflats.

This study area is controlled by a monsoon climate. The annual mean temperature is 14.1 °C and annual precipitation is around 1100 mm (Yang, 1982). The surficial sediment is composed mainly of silts and sandy silts (Wang and Ke, 1997). Typically, the intertidal flat is covered with *Suaeda glauca* Bunge, *Suaeda maritime* Dumort and *Spartina anglica* over the upper intertidal area; mud flats, mixed flats and silt-sand flats form the mid-lower intertidal areas (Yang, 1982; Ren, 1986). The Wanggang River enters the sea in the south of the study area, but a tidal-sluice gate (i.e., Wanggang Dam) was built to prevent saline water intrusion (Fig. 1B). Hence, the river discharge is limited and is controlled artificially. A large harbor was constructed for freight traffic from Dafeng Harbor, in the north of the study area. Since the intertidal flat represents a potential land source, it was reclaimed by building dykes (or sea walls) in 1978, 2000 and 2008. The reclamation has resulted in a considerable reduction in the intertidal area (Fig. 1B, C). The average width of intertidal flat was more than 10 km before 1978; however, it has decreased to 2.9 km, by 2008 (see below, Fig. 12). Moreover, *Suaeda glauca* Bunge and *Suaeda maritime* Dumort are disappearing and *Spartina* has become the dominant salt marsh species over the upper intertidal flat (Chung et al., 2004).

3. Methods

3.1. Hydrodynamic measurements

In situ measurements were undertaken using a custom-made Valeport MIDAS400 Data Acquisition System (abbreviated as MIDAS400 in the following text), at station M03 on the mid-lower intertidal flat on July 3–10, 2003. Measurements were also undertaken at Station C06 (at a creek mouth) on the *Suaeda salsa* covered upper intertidal flat on May 14–16, 2006 (Fig. 1B). Additionally, long-term water level measurements were obtained from two tidal gauge stations, i.e. WG03 (using a tide staff, in July, 2003) and DF05 (using a Valeport 740 Tide Gauge, from June 16 to July 25, 2005).

The MIDAS400 consists of six pairs of Model 802 EM (electromagnetic) current meters and Seapoint turbidity sensors, as well as conductivity, temperature and pressure sensors with logging electronics (Wang et al., 2006). The EM and turbidity sensors were

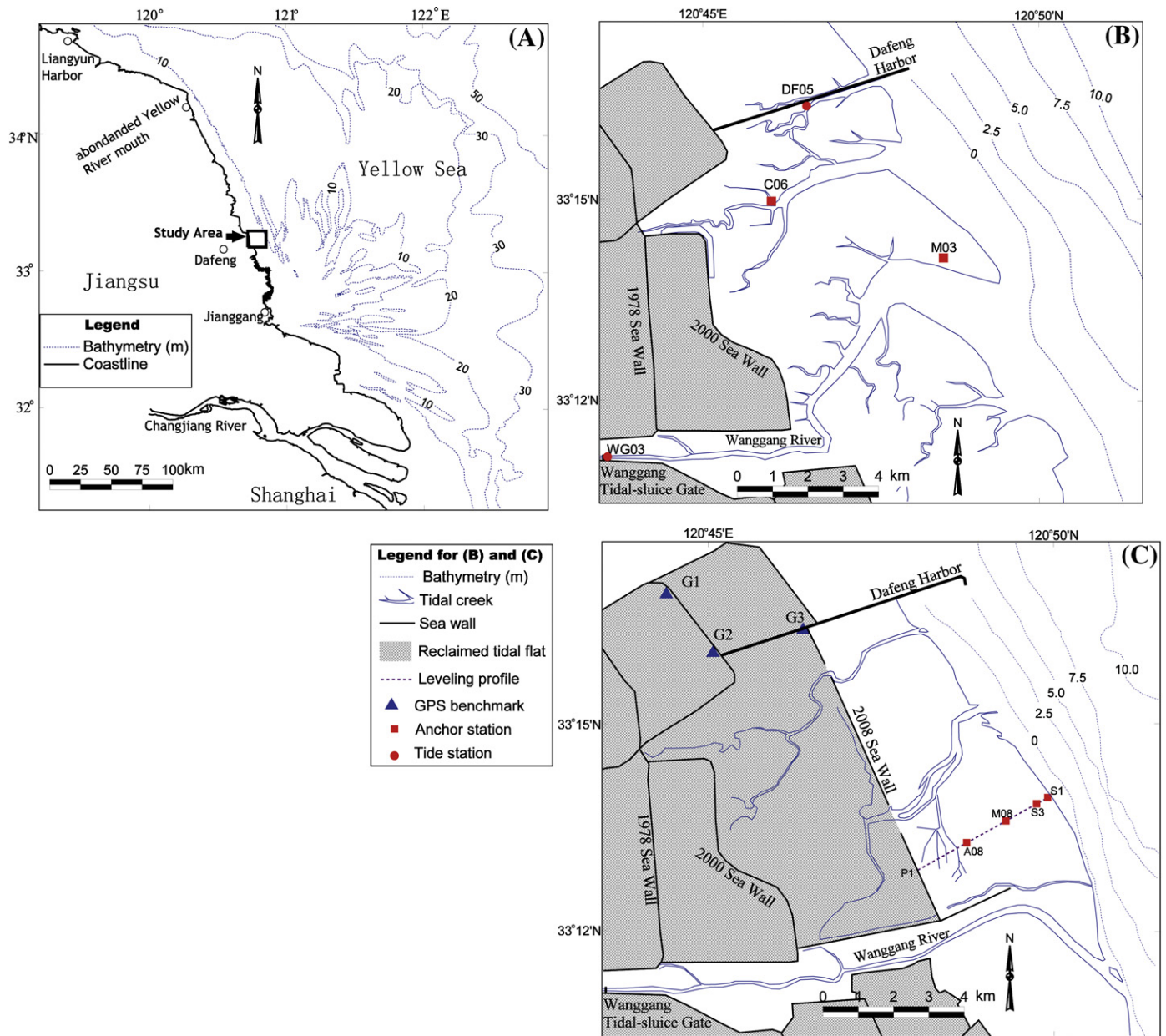


Fig. 1. Maps showing the study area and the location of the intertidal flats at Dafeng, Jiangsu, China (A: on the basis of the 1995 chart; B: on the basis of a 2003 Landsat5 TM image; and C on the basis of a 2008 Landsat5 TM image). The squares show the observation sites for hydrodynamic measurements, whilst circles show the sites for the water level measurements. The bathymetry were undertaken in 1979 (A and B) and 2006 (C), in meters.

mounted on a stainless steel frame, with poles that penetrated the intertidal flat surface by more than 1 m to provide stability. The position of the sensors is adjustable. In order to collect the water samples simultaneously with the MIDAS400 measurement, a 3 m high platform (higher than the local high water level) was constructed above the intertidal flat using strong bamboo poles.

During the measurements, six pairs of EM and turbidity sensors were installed at 0.08–1.56 m above the seabed at Station M03 and 0.38–1.12 m at Station M08. The distances between the adjoining sensors increased logarithmically from the bottom upwards, and the sampling rate was set at 4 Hz. Water samples of around 1 L in volume were collected every 10–20 min, from 3 to 5 layers in the water column, using a water sampler from the platform. In addition, bottom sediment samples were collected and the geometric parameters of the ripples on the flat surface were measured when the intertidal flat was exposed. A Valeport, UK Model 740 portable water level recorder was deployed on the surface of the bed near the platform to obtain a time-

series of water level, for comparison with the measurements of the MIDAS-400 pressure sensor.

Three sets of instruments, i.e., a YSI/SonTek ADV Ocean, MIDAS400 and a TRDI WHS 1200 kHz ADCP, were deployed along the profile P1 to measure high-resolution sediment dynamics across the intertidal flats during May 5–12, 2008 (Fig. 1C). The ADV Ocean was deployed with D&A OBS-5+ on the upper intertidal flat (Station A08) with the sensor being installed at 0.18 m above the bed. The ADCP was deployed on a floating body with radio communications and power supplies, together with a SBE26 for wave measurement, at the site S1 during May 5–7 and site S3 during May 9–11, 2008, both near mean low water level (MLWL). The transducer of the ADCP was placed at 0.1 m below the sea surface and a high-resolution mode was selected to obtain 0.05 m water cells of current velocity structure. The MIDAS400 was deployed at Station M08, between the ADV and ADCP sites on May 5–11, 2008 (Fig. 1C). During the measurement periods, water samples were collected at different depths to calibrate the OBS-5+, MIDAS turbidity sensors and ADCP

acoustic signals. In addition, a weather instrument, Davis Instruments Vantage Pro2 was deployed on the middle intertidal flat near MIDAS400.

3.2. Surficial sediment sampling and bed leveling

At each station, surficial sediment samples were collected, for the measurement periods of 2003, 2006 and 2008. A Magellan Z-MAX GPS RTK (a differential GPS system) was used to obtain high accuracy elevation and positional data for the intertidal flat. The GPS RTK has a static accuracy of $5 \text{ mm} + 0.5 \text{ ppm}$ for horizontal position and $10 \text{ mm} + 0.5 \text{ ppm}$ for elevation measurements. The dynamic accuracy decreased to 10 mm in the horizontal position and 20 mm for elevation. In order to obtain the elevation with reference to the local datum, three GPS benchmarks (G1, G2 and G3 in Fig. 1C) were determined. The seabed leveling was undertaken along a profile (P1 in Fig. 1C) from the upper to the lower intertidal flat on May 13, 2008 and December 25, 2008. Surficial sediment samples were collected along this profile at 100–200 m intervals at the leveling sites.

3.3. Laboratory analysis and data processing

Each of the water samples was divided into two sub-samples. One (0.2–0.4 L in volume) was filtered through a $0.45 \mu\text{m}$ filter (product of the Second Institute of Oceanography, State Oceanic Administration, China), and dried in an oven (temperature 40°C) for 48 h to determine suspended sediment concentrations (SSC). In order to remove the influence of filter mass changes during the filtration experiment, two filtration membranes were used for every 10 water samples. The blank filtration membranes were used to calibrate all the remaining filtration membranes. The second sub-sample was analyzed by the Malvern Mastersize 2000 laser granulometer (measuring range $0.02\text{--}2000 \mu\text{m}$, with a duplicate measurement error of $<3\%$) to obtain the grain size distribution curves of the suspended material. The surficial sediment samples were pretreated by dispersion, and then analyzed using the Mastersize 2000 laser granulometer. The grain size parameters were calculated from the distribution curves using moment statistics

(McManus, 1988). Grain size trend analysis (Gao and Collins, 1992; Gao, 1996) was carried out to infer the pattern of net sediment transport pathways.

The instantaneous water level data measured by the MIDAS400 pressure sensor were grouped into 256 data sets, each containing a number (i.e. 1024) of wave bursts. The tidal water level was calculated by averaging the first and last third of the bursts. The pressure data was de-trended to remove the tidal variation during the bursts, so that all wave calculations are referenced to the same level. Furthermore, Fourier transforms were carried out to provide pressure spectra. On this basis, all of the raw data were treated with reverse Fourier transformation to back calculate the surface elevation for every sample in the bursts. Thus, the wave parameters, e.g. significant and maximum wave height, mean wave period, and total wave energy, were obtained (Green et al., 1997).

The suspended sediment flux is expressed by

$$F = \int_T \int_H C(z, t) V(z, t) dz = \sum_j \Delta t_j \left(\sum_i (\Delta z_i C_{i,j} V_{i,j}) \right),$$

where $F (\text{kg m}^{-1})$ is the flux through a unit width with water depth of $H (\text{m})$ during time scale of $T (\text{s})$; $C(z, t)$ and $V(z, t)$ are the SSC and the velocity component at the height z and at the time t , respectively; $C_{i,j}$ and $V_{i,j}$ represent the SSC and the velocity component of i -th water layer (with water cell thickness of Δz_i) during the period of Δt_j (j is the sign of time), respectively. The flood, ebb and net suspended sediment flux represent integral value during the flood period, the ebb period and the entire tidal cycle, respectively.

4. Results

4.1. Characteristics of the tidal regime

Water level data were obtained at Station WG03 on the seaward side near the Wanggang Tidal-sluice Gate in July, 2003 (Fig. 2A). Although the water levels show some semi-diurnal components,

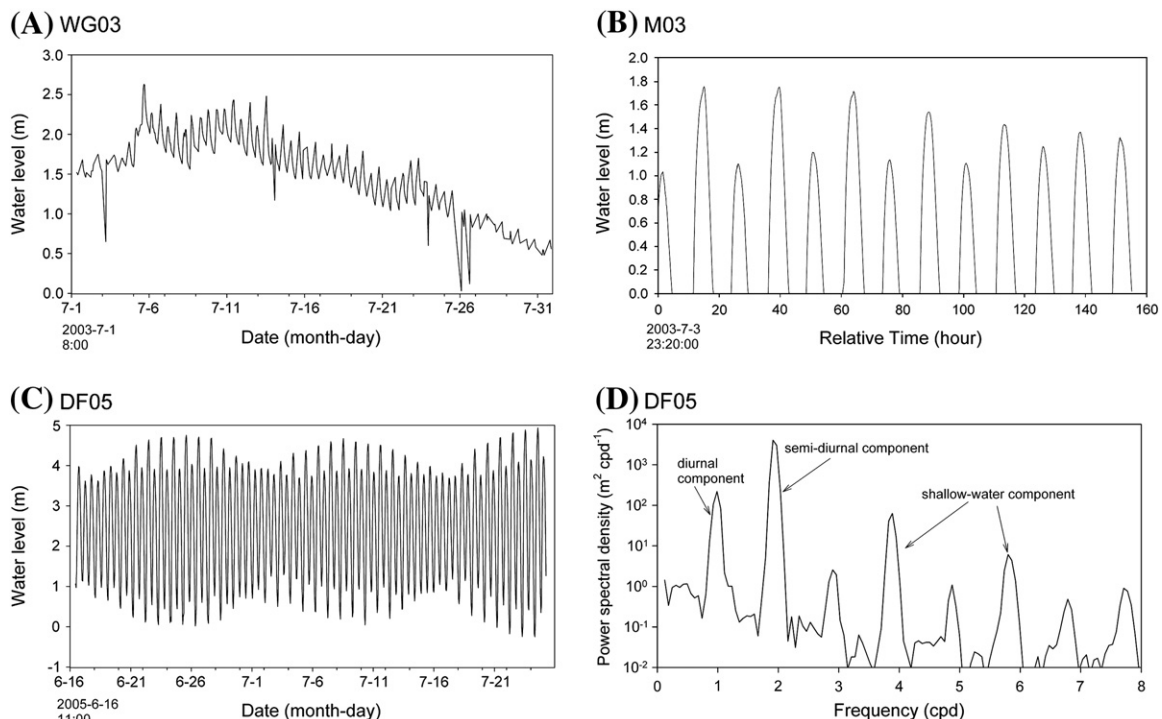


Fig. 2. Time-series of water level measured at Stations (A) WG03 in July, (B) M03 over the intertidal flat on July 3–10, 2003, (C) DF05 on June 16 to July 25, 2005 (local datum) and (D) power spectral density estimated by harmonic analysis at DF05 (cpd means cycle per day).

Table 1

Tidal components near Dafeng Harbor derived by harmonic analysis on 39 days water level data at DF05 from June 16 to July 25, 2005.

Tide	Amp (m)	Amp error	Phase (°)	Phase error	SNR
M2	1.69	0.02	321.46	0.39	12,000
S2	0.53	0.01	37.44	1.61	1400
N2	0.33	0.01	306.47	2.66	580
K1	0.27	0.01	56.49	2.86	480
O1	0.21	0.01	348.59	3.70	270
M4	0.19	0.02	143.43	5.56	120

there is a general decreasing trend over the sampling period with some peaks. In addition, the tidal range is abnormally small since the tidal-sluice gate was opened for river drainage during the ebb and consequently increased the low water level. The distorted tidal level data are therefore not suitable for harmonic analysis. The asymmetrical semi-diurnal tide was observed over the intertidal flat at station M03 on July 3–10, 2003 (Fig. 2B). The submergence time was between 5.3 and 6.7 h, with flood and ebb durations being 2.2–3.5 h and 3.2–3.9 h, respectively. The emergence time was between 5.8 and 7.1 h. Similar patterns were observed at Station M08 on May 5–12, 2008 (Fig. 4). Since the water level cannot be measured when the intertidal flat is exposed, tidal harmonic analysis is not suitable for the data measured over the intertidal flat.

The code for harmonic analysis (Leffler and Jay, 2009) was applied to the water level data obtained at Station DF05 in June and July, 2005 (Fig. 2C). The results show that this area is dominated by the M2 tide, with its amplitude being 1.69 m (Table 1). The semi-diurnal constituents of M2, S2 and N2 are dominant over the other constituents, which have a large power spectral density of $10^{3-4} \text{ m}^2 \text{ cpd}^{-1}$, in terms of the tidal amplitude (Fig. 2D). The diurnal and shallow-water components have amplitudes of approximately 0.2 m and a power spectral density of $10^{1-2} \text{ m}^2 \text{ cpd}^{-1}$.

4.2. Weather and wind wave conditions

Weather data were obtained from the city of Dafeng on July 3–10, 2003, and at Station M08 on May 5–11, 2008, for the same periods as the

hydrodynamic measurements. Because this weather station was located on land with rough terrain, the winds were lower than those measured offshore (Table 2). WNW winds were observed, with a maximum speed of 5.3 ms^{-1} on July 4, whilst a storm was recorded on July 5, 2003, with heavy rain of $116.4 \text{ mm day}^{-1}$. At the weather station deployed at M08 in May 2008, maximum wind speeds of 9.8 ms^{-1} were from the east when the intertidal flat was inundated and they were 13.4 ms^{-1} from the north when the intertidal flat was exposed.

Strong winds can generate large waves along the coast. During the measurements on July 3–10, 2003, at M03, the significant wave height, as derived from the MIDAS400 high frequency pressure data, ranged from 0.30 to 0.50 m (Table 2). Since maximum water depths ranged between 1.03 and 1.75 m, these waves can generate a peak orbital velocity up to 0.3 m s^{-1} (Wang et al., 2006). Hence, the near-bed shear stress due to combined wave-current interaction could reach up to 1.17 Nm^{-2} (see below), which was sufficient to disturb the surficial sediment over the intertidal flat and result in sediment transport (cf. Jia et al., 2006). The wave period was 3–5 s. A significant relationship existed here between wind speeds and wave heights, for the measurements of 2003 ($R^2=0.65$, $p<0.05$) and 2008 ($R^2=0.68$, $p<0.05$), which indicates that the waves were predominantly the result of local winds rather than swells from offshore. Under calm weather, the significant wave heights were 0.01 m and 0.03 m during the tidal cycles on May 9–10 and May 10–11, 2008, respectively (M08).

4.3. Tidal currents

The hydrodynamic parameters were measured along a profile across the intertidal flat from the upper to the lower reaches in May, 2008 (Fig. 1C). The measurements of May 6, 2008, reveal a typical pattern of tides and tidal currents (Fig. 3). The flood arrived at Station A08, which represent the upper tidal flat, at 10:15 (Beijing time) with a current speed of 0.04 ms^{-1} towards the northwest (Fig. 3A). The maximum velocity was 0.11 ms^{-1} at 11:40 during the flood and 0.19 ms^{-1} at 13:40 during the ebb. The high water level was 0.72 m at 12:30 (Fig. 3D), and even during slack water there were some currents, which were directed towards the north and contributed to the formation of an NNW residual current of 0.09 ms^{-1} .

Table 2

Wind waves, climate and seabed sediment grain size.

Station	Date (time)	Max. water depth (m)	Significant wave height (m)	Wind speed (m s^{-1})/direction	Precipitation (mm day^{-1})	Median grain size of surficial sediment
M03	07/03–04/2003 (23:15–4:35)	1.03	0.44	4.2/ESE	0.0	3.64 Φ (80 μm)
	07/04/2003 (11:30–18:10)	1.75	0.40	5.3/WNW	0.0	3.64 Φ (80 μm)
	07/05/2003 (0:00–5:30)	1.06	0.33	2.8/NW	116.4	3.64 Φ (80 μm)
	07/09/2003 (3:35–9:50)	1.21	0.31	2.9/E	0.0	4.32 Φ (50 μm)
	07/09–10/2003 (15:40–22:05)	1.36	0.30	1.6/WNW	0.0	4.32 Φ (50 μm)
	07/10/2003 (4:50–11:15)	1.30	0.50	4.7/NE	0.0	4.32 Φ (50 μm)
	05/05–06/2008 (20:22–2:47)	1.71	0.33	7.0/S	0.0	3.80 Φ (72 μm)
M08	05/06/2008 (8:44–15:26)	2.05	0.40	8.1/S	0.0	3.80 Φ (72 μm)
	05/06–07/2008 (20:57–3:36)	1.79	0.32	5.6/SE	0.0	3.80 Φ (72 μm)
	05/09–10/2008 (22:56–5:45)	1.77	0.01	3.0/NE	0.0	3.60 Φ (82 μm)
	05/10/2008 (11:18–19:03)	2.51	0.17	6.1/SE	0.0	3.60 Φ (82 μm)
	05/10–11/2008 (23:40–6:22)	1.85	0.03	5.8/S	0.0	3.60 Φ (82 μm)
	05/11/2008 (12:12–20:14)	2.30	0.43	9.8/E	0.0	3.60 Φ (82 μm)

Note: The wind and rain for M03 were obtained from the city of Dafeng.

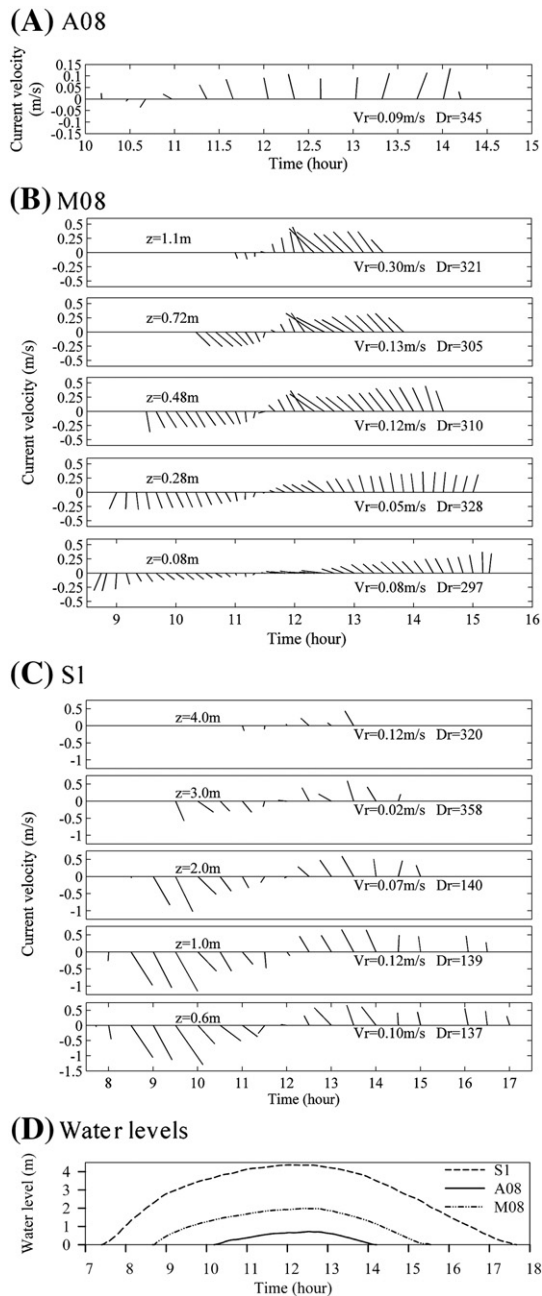


Fig. 3. Time-series of current velocity vectors (A, B and C) and corresponding water levels (D) over the intertidal flat measured at Stations A08, M08 and S1 on May 6, 2008. The vector direction is based on the Darrh coordinate, i.e. N (north) towards top and E (east) and towards right. Key: z = height above the seabed (m); V_r = residual current speed (m s^{-1}); and Dr = residual current direction ($^\circ$).

According to the measurements from the EM sensor (located at 0.08 m above the seabed) deployed on the middle tidal flat, the current velocity during the initial flood was greater than 0.3 m s^{-1} and was directed towards the southwest at around 8:44 on May 6 (Fig. 3B). This initial flood surge over the intertidal flat was the same as that observed within the tidal creeks, which corresponded to a high rate of water level rise (Wang et al., 1999). This surge, with high SSCs (see below; Fig. 4) was similar to the 'turbid fringe' observed elsewhere by Green et al. (1997). The current then decreased and the flow gradually rotated anticlockwise to the southeast, both in the bottom and upper layers. Minimum current speeds occurred at 11:10–11:25 before the highest water level. The occurrence of low velocities was delayed near the water surface, compared with the near-bed layer, when the

current had a speed of below $0.05\text{--}0.10 \text{ m s}^{-1}$, directed seaward. During the ebb, the current velocity increased towards the west (two bottom layers) or northwest (three upper layers) and rotated counterclockwise. It reached the peak value at 16:20–16:30, when the velocities ranged between 0.54 m s^{-1} and 0.63 m s^{-1} from mid-layer (0.48 m above the seabed) to the water surface. Reduction in the current velocity during the middle to late ebb was not significant; it remained stable at about 0.30 m s^{-1} . During the final stage of the ebb, the flow direction changed to the north and northeast (i.e. towards the sea).

On the lower intertidal flat, i.e. at Station S1 lying close to the MLWL, the hydrodynamics became more intense, due to deeper water and relatively lower bottom friction. The peak current velocity occurred during the mid-flood at around 9:30 (Fig. 3C). At this time, the velocity decreased from the bottom upwards, i.e. reducing from 1.4 m s^{-1} at 0.6 m to 0.61 m s^{-1} at 3.0 m above the seabed. Subsequently, the tidal current rotated anticlockwise towards the southeast and high water slack occurred at 12:30 with the highest water level being 4.37 m above the seabed (Fig. 3D). The ebb current was much weaker than the flood current. The maximum current speed was about 0.70 m s^{-1} during the early ebb, with a northwesterly direction.

For an ideal standing wave the phase difference between the water level and the tidal current is 90° , whereas for a progressive wave this difference is 0° (Johns, 1983). The above observations show that the current velocity minima were 0.5–1 h ahead of the high water slack over the mid-lower tidal flat (Fig. 3). This phenomenon indicates that the tidal waves over the intertidal flats were not purely standing waves; they contained a component of progressive waves.

The tidally induced residual current was characterized by velocity asymmetry due to tidal wave deformation. The measurement at Station M08 shows that the residual currents at different heights above the bed were all landward (northwest) and were lowest over the lower part of the water column. However, the residual current reveals different features between the upper and lower layers at Station S1, directed landward within the upper layer, but seaward within the lower layer. This pattern is apt to transport upper fine-grained (cf. Fig. 7) sediment landward and lower coarse-grained sediment seaward. In addition, the residual current was generally stronger over the middle intertidal flat than over the upper and lower intertidal flats (See below, Table 4). The measurements undertaken on July 5, 2003, also show that extreme weather conditions (e.g. rainstorm runoff) may be an important factor intensifying the residual currents (Wang et al., 2006). Based upon the combined wave-current models proposed by van Rijn (1993) and Soulsby (1997), the near-bed shear stress was calculated from the wave parameters obtained, which results in bottom shear stress reaching 1.17 N m^{-2} (much higher than the 0.48 N m^{-2} of pure tide-induced shear stress) on July 5, 2003. The superimposed effect of waves on tidal currents over the intertidal flat can result in strong hydrodynamics and complex interactions between the physical processes.

4.4. Suspended sediment concentrations and transport rates

Water samples were collected to calibrate the turbidity measurements (i.e. at Stations A08, M03 and M08) and acoustic backscatter (i.e. at Stations S1 and S3). Linear regressions were performed to provide calibrations (Table 3) permitting the construction of SSC profiles.

In general, the depth-averaged SSC over a complete tidal cycle is highest over the lower intertidal flat (i.e. Stations S1 and S3), reduced on the mid intertidal flat (i.e. M08), and lowest on the upper reaches (Fig. 4). Nevertheless, at high tide, the SSC is high on the middle flat (i.e. green curve in Fig. 4). At Station S1 measured on May 5–7 (spring tide), the currents were strong with along coast current magnitudes (i.e. V_a) of up to 1 m s^{-1} , resulting in high SSCs of 226–3000 mg L^{-1} .

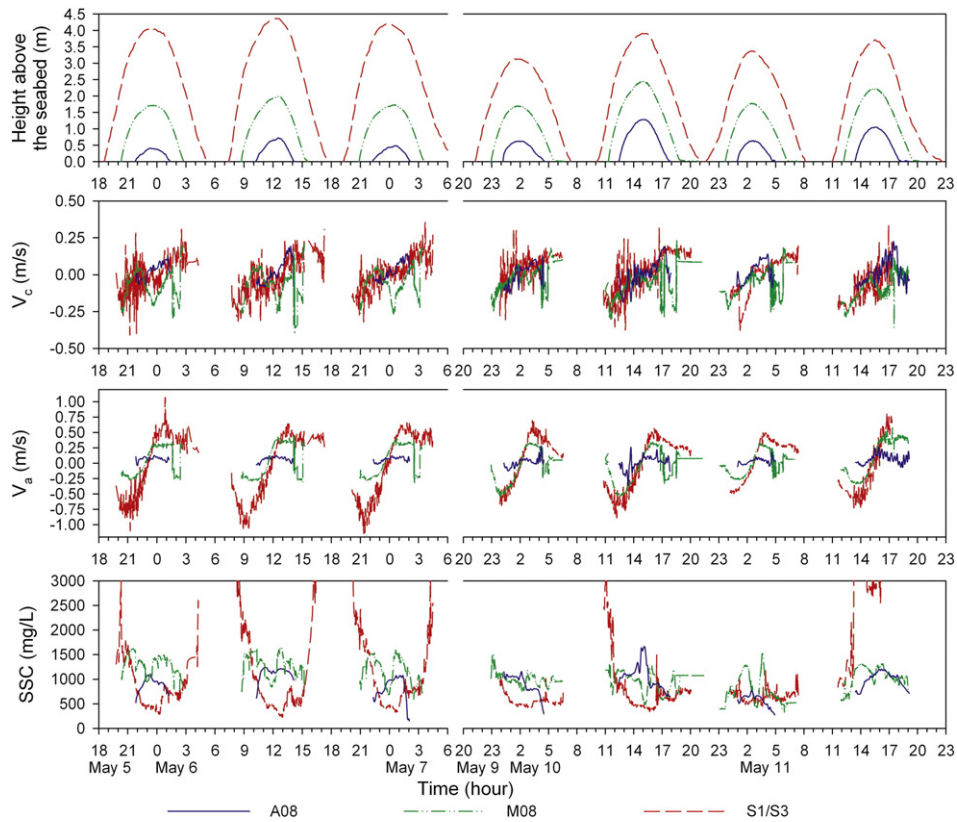


Fig. 4. Time-series of water depth, depth-averaged current velocity and SSC measured at Stations A08 (blue solid-line), M08 (green dash-dot-line), S1 (red dash-line, between May 5 and 7) and S3 (red dash-line, between May 9 and 11) in May, 2008. V_a and V_c are the current velocity components along and across the intertidal flat, respectively.

Two peaks of SSC were present at the beginning and the end of the tidal cycle, corresponding to relatively high current velocities and indicating strong resuspension. However, even when the current velocity was slightly higher at the station S3 than that of the middle intertidal flat (i.e. M08), the SSC were generally lower at Station S3 during the tidal cycles on May 9–10 and 11, 2008 (close to neap tide).

Over the middle intertidal flat (M08), the SSCs were characterized by several peaks over a tidal cycle (Fig. 4). For the most part the high SSC values (i.e. 800–1600 mg L⁻¹) are associated with high current velocities at the mid-flood and mid-ebb, indicating the occurrence of significant resuspension. The SSC then decreases to <500 mg L⁻¹ due to the settling during slack water before the reversal of the tidal current. In addition, wind waves could play an important role in high SSCs. A peak in SSC (more than 1500 mg L⁻¹) (Fig. 4) occurred during strong waves (significant height of 0.43 m) during the tidal cycles on May 11 (Table 2).

Fig. 5 shows that the SSC increased significantly (with a concentration of more than 1200 and 1600 mg L⁻¹ in July 4 and 10, 2003, respectively) due to an observed initial flood surge and intense turbulent mixing within the water column by the frontal flow (water depth of 0.1–0.3 m). At the initial stage of the flood, the rate of water level change was high, inducing significant shear; this pattern is consistent with observations made elsewhere in tidal creeks (Wang et al., 1999; Yang

et al., 2003). During slack water and before the turn of the tidal current, the SSC decreased rapidly to less than 400 mg L⁻¹ above a depth of 0.5 m, associated with a water level change rate close to zero. When the water level change rate increased at the beginning of the ebb, the bottom shear stress and SSC increased again to generate another SSC peak.

Over the middle part of the intertidal flat (i.e. Station M08), stratified SSCs resulted from settling and weak turbulence where the across-flat velocity was less than 0.2 ms⁻¹ on May 6, 2008 (Fig. 6A). However, the tidal current was strong during the initial flood on May 10, 2008. The water column had been well mixed resulting in uniform SSCs within the water column. The SSCs reached 1800 mg L⁻¹ and the cross-flat velocity was in excess of 0.3 ms⁻¹, which was inclined to favor onshore sediment transport. Such a pattern was not present during the ebb.

Station S1 is located close to the lowest boundary (low water level) of the intertidal flat adjacent to the sea. The maximum water depth was 4.3 m with a high rate of change of water level during the flood (Fig. 6B). Thus, the current velocity increased rapidly to above 1.1 ms⁻¹ at 9:00 (May 6, 2008); this, in turn, resulted in intense resuspension and high SSCs near the seabed (e.g. >2000 mg L⁻¹). A similar pattern was also present at Station S3, located within an area onshore of S1. However, the current velocity was relatively low during the ebb, corresponding to lower and more uniform SSC levels within

Table 3
In situ water samples calibrated equations for suspended sediment concentration (mg L⁻¹) estimation.

Stations	Date	Location	Equation
A08	May 5–12, 2008	120°48'41.2", 33°13'14.4"	SSC = 3.155 T (R = 0.96, n = 19)
M03	July 3–9, 2003	120°48'33.4", 33°14'07.0"	SSC = 0.632 T (R = 0.95, n = 154)
M08	May 5–12, 2008	120°49'17.5", 33°13'35.7"	SSC = 0.688 T (R = 0.92, n = 88)
S1	May 5–8, 2008	120°49'53.7", 33°13'55.9"	log(SSC) = 0.05 E _i - 2.16 (R = 0.92, n = 29)
S3	May 9–12, 2008	120°49'44.1", 33°13'50.6"	log(SSC) = 0.03 E _i - 0.04 (R = 0.90, n = 27)

Note: R denotes the correlation coefficient and n the number of water samples; T is the turbidity (V) and E_i is the acoustic backscatter (dB).

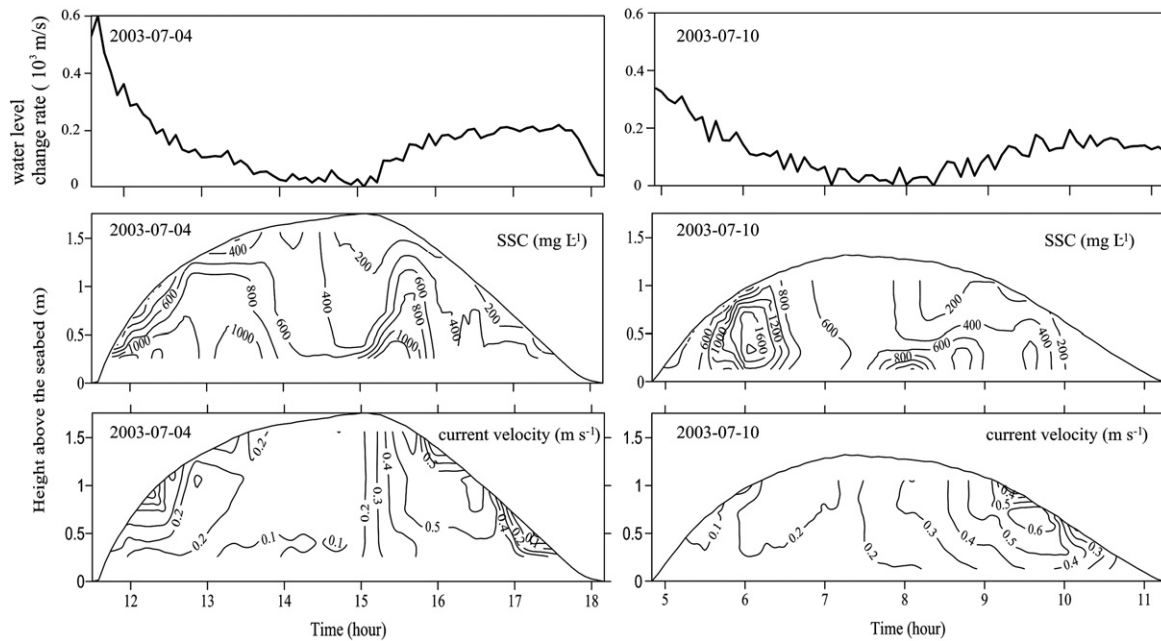


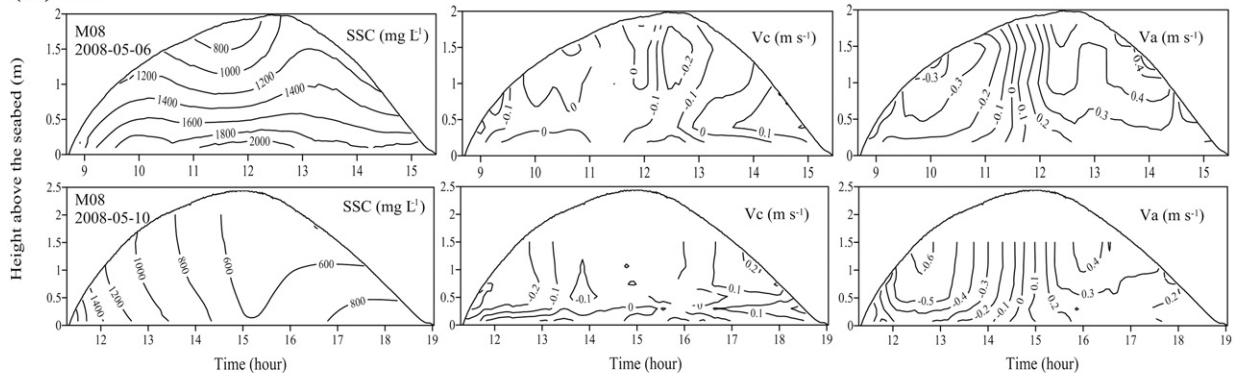
Fig. 5. Time-series of water level change rate and SSCs measured at Station M03 in July, 2003.

the water column. At slack, when the water level was highest, the current velocity was less than 0.1 m s^{-1} with correspondingly the lowest SSC due to settling.

Measurement at station M08 shows that the mean size of suspended sediment was $6.3\text{--}6.8 \Phi$ on May 10, slightly coarser than that (i.e. 6.2--

7.4Φ) on May 6, 2008. This difference indicates that coarser sediment could entrain on May 10 (after the spring tide on May 6). Furthermore, the suspended sediment was finer than the seabed sediment (see below, Fig. 9), indicating hydraulic sorting. The mud content could exceed 85% of the suspended sediment (Fig. 7), considerably higher than the typical

(A) M08



(B) S1 and S3

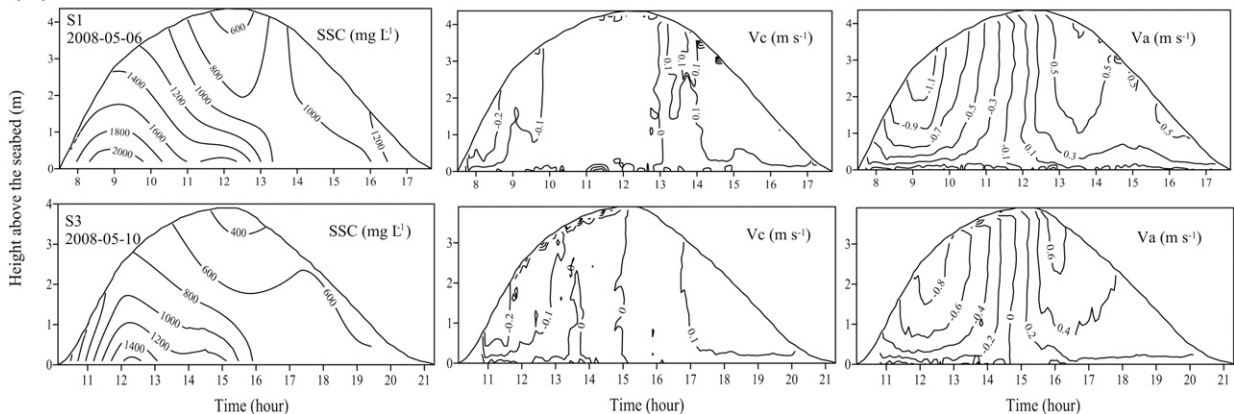


Fig. 6. Time-series of SSCs and current velocity components (V_a and V_c are the velocity along and across the intertidal flat, respectively) measured at Stations (A) M08 and (B) S1, S3 in May, 2008.

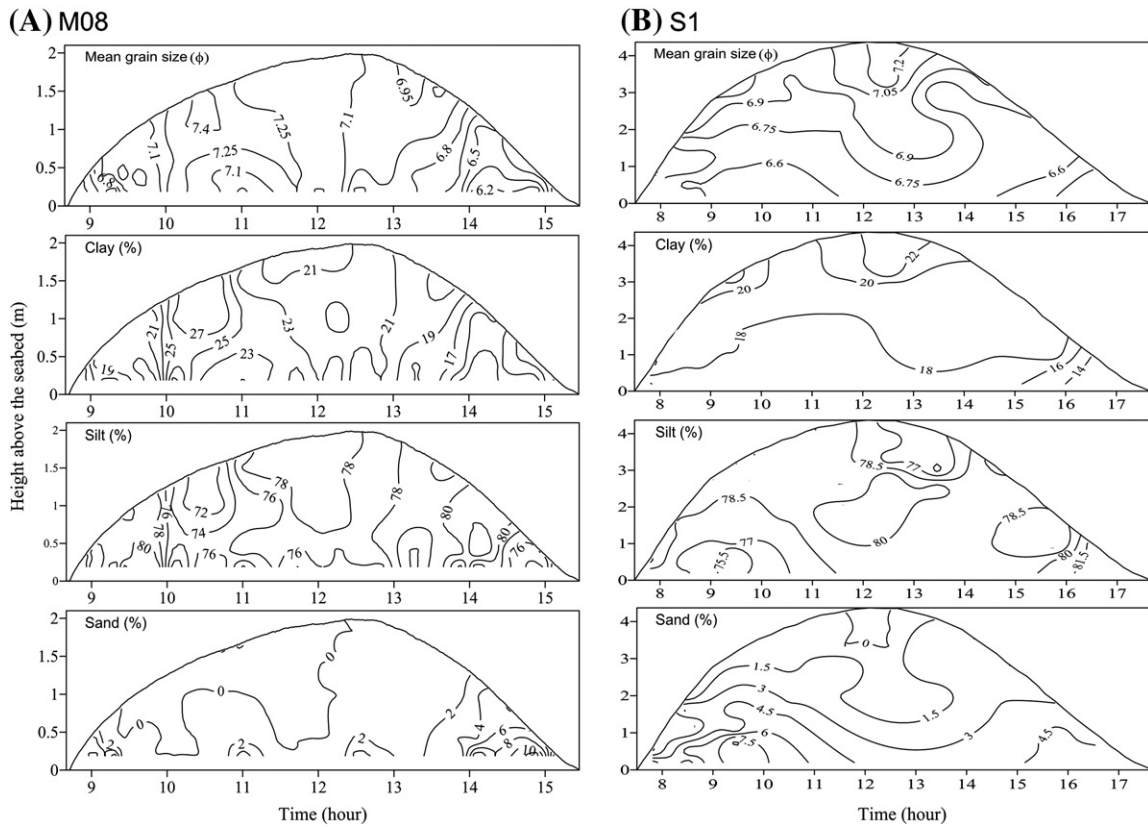


Fig. 7. Grain size parameters of suspended sediment within the water column at Stations (A) M08 and (B) S1 on May 6, 2008.

percentage of 40% found for the local seabed sediment. The grain size distribution of suspended sediment shows a single peak with a fine tail (Fig. 8) with skewness of 1.6–2.1. The mean grain size of the suspended sediment was also consistently finer during the flood (e.g. 7.42 Φ , Fig. 8) than the ebb (e.g. 6.48 Φ , Fig. 8), while the silt content was almost symmetrical during a tidal cycle. This implies that the occurrence of silt, which only needs a relatively low shear stress to be entrained into the water column, dominates during both the flood and ebb. Nevertheless, the clay content was high during the flood (up to 27% at 10:30 on May 6, Fig. 7A). The clay contents were 28.2% and 21.7% without any sands at Stations M08 and S1 during the flood, respectively (Fig. 8). However, the

clay content was less than 17.4% with a sand content of above 3% during the ebb. These results show that there was a net transport of fine-grained sediments landward and coarser sediments seaward over the middle intertidal flat. At Station S1, the grain size of the suspended sediment is marginally finer during the flood and slack water periods than during the ebb (Fig. 7B). Hence, the results outlined above provide additional evidence for onshore transport of clay-sized sediment during the flood and an offshore transport of sands during the ebb.

The net suspended sediment fluxes increased from the upper to the lower intertidal flat during the tidal cycle, with a strong residual current present on the middle intertidal flat (Table 4). The magnitudes of the

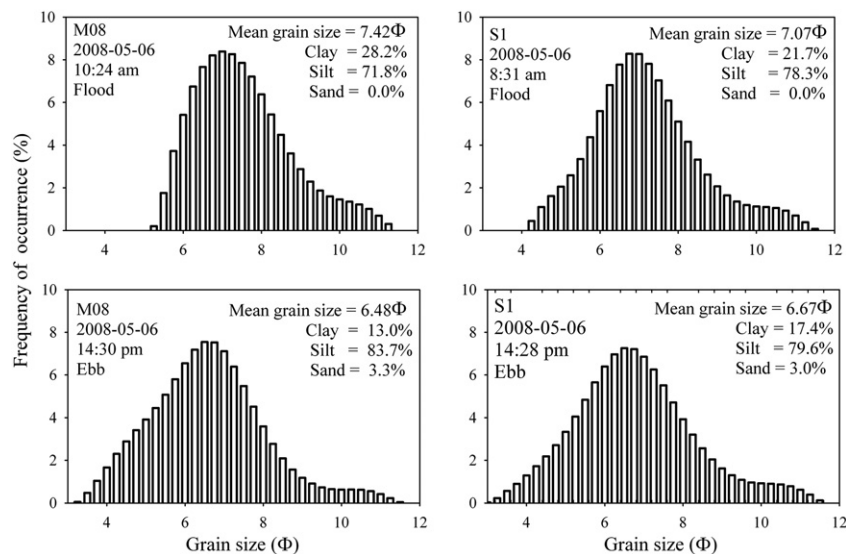


Fig. 8. Grain size distribution of suspended sediment collected at Stations M08, S1 on May 6, 2008.

Table 4

Suspended sediment fluxes during tidal cycles measured at the intertidal sites.

Station	Date (time)	Max. water depth (m)	Suspended sediment fluxes ($\times 10^3 \text{ kg m}^{-1}$) / direction ($^\circ$)					V_r (m s^{-1})
			Flood	Ebb	Lateral	Longitudinal	Net	
A08	5/5–6/2008 (21:50–1:22)	0.40	0.10/321	0.19/7	0.10	0.25	0.27/351	0.02
	5/6/2008 (10:11–14:13)	0.72	0.39/313	0.34/22	0.16	0.61	0.64/345	0.03
	5/6–7/2008 (22:15–2:10)	0.48	0.16/325	0.18/15	0.11	0.29	0.31/352	0.01
	5/7/2008 (10:12–15:12)	1.07	0.54/293	0.69/4	0.06	1.00	1.01/333	0.05
	5/7–8/2008 (22:45–2:41)	0.47	0.15/316	0.19/5	0.07	0.30	0.31/343	0.02
	5/8/2008 (10:49–16:24)	1.34	0.98/189	1.19/4	0.04	0.23	0.23/340	0.03
	5/8–9/2008 (23:10–3:47)	0.56	0.16/216	0.41/14	0.13	0.23	0.26/360	0.00
	5/9/2008 (11:26–17:36)	1.36	1.29/175	0.53/21	−0.14	−0.83	0.84/160	0.12
	5/10/2008 (0:11–4:35)	0.62	0.199/195	0.205/14	0.003	0.005	0.006/5	0.11
	5/10/2008 (12:20–17:55)	1.28	0.44/209	0.72/356	−0.06	0.42	0.43/322	0.11
	5/11/2008 (0:53–5:00)	0.64	0.04/276	0.17/23	0.10	0.13	0.16/8	0.05
	5/11/2008 (13:20–19:08)	1.04	0.31/304	1.04/357	0.34	1.20	1.24/346	0.04
	07/03–04/2003 (23:15–4:35)	1.03	0.54/357	1.85/44	2.02	0.99	2.25/34	0.26
	07/04/2003 (11:30–18:10)	1.75	1.07/184	2.13/41	1.41	−0.21	1.42/68	0.13
	07/05/2003 (0:00–5:30)	1.06	0.48/15	0.89/48	1.21	0.53	1.32/36	0.21
	07/09/2003 (3:35–9:50)	1.21	0.62/171	0.99/52	0.76	−0.45	0.88/91	0.18
M03	07/09–10/2003 (15:40–22:05)	1.36	0.88/172	1.10/50	0.76	−0.63	0.99/100	0.17
	07/10/2003 (4:50–11:15)	1.30	1.10/184	1.56/67	0.93	−1.10	1.44/110	0.16
	05/05–06/2008 (20:22–2:47)	1.71	2.02/191	5.38/317	−2.57	3.70	4.51/295	0.12
	05/06/2008 (8:44–15:26)	2.05	2.58/169	6.56/322	−1.75	4.05	4.41/307	0.11
	05/06–07/2008 (20:57–3:36)	1.79	1.74/197	4.65/324	−1.74	3.44	3.85/303	0.11
M08	05/09–10/2008 (22:56–5:45)	1.77	4.60/162	2.95/337	−0.63	−1.65	1.76/171	0.05
	05/10/2008 (11:18–19:03)	2.51	7.75/166	4.84/335	−1.73	−2.63	3.14/183	0.04
	05/10–11/2008 (23:40–6:22)	1.85	2.79/178	2.85/337	−0.94	0.36	1.01/261	0.04
	05/11/2008 (12:12–20:14)	2.30	4.88/181	8.65/322	−3.74	4.39	5.77/290	0.12
	05/09–10/2008 (20:46–7:26)	3.15	13.77/157	6.15/342	−0.44	−7.64	7.66/153	0.05
	05/10/2008 (9:50–21:35)	3.95	19.45/162	9.16/347	−1.48	−10.24	10.34/158	0.02
	05/10–11/2008 (21:35–8:30)	3.37	11.11/168	8.48/341	−1.80	−2.26	2.89/189	0.03
S3	05/05–06/2008 (19:08–4:24)	4.11	24.71/157	15.80/340	−0.40	−8.95	8.96/153	0.02
	05/06/2008 (7:30–17:40)	4.37	38.51/160	20.11/346	−0.85	−18.66	18.67/153	0.03
S1	05/06–07/2008 (19:12–5:58)	4.18	35.11/158	24.88/337	−1.66	−10.11	10.24/159	0.01

Note: Lateral and longitudinal denote the transport direction across (offshore “+” and onshore “−”) and along (northward “+” and southward “−”) the tidal flat, respectively. V_r is the residual current speed (m s^{-1}).

fluxes during the flood and the ebb were similar at different stations, but the patterns between lateral and longitudinal fluxes at these stations were different.

At Station A08 over the upper intertidal flat, the fluxes reached a magnitude of 10^2 kg m^{-1} during the flood and ebb, with the sediment transport directions being highly variable on the flood (Table 4). The fluxes were predominantly toward the northeast during the ebb. Additionally, the longitudinal components were usually several times than that of the lateral components, mainly towards the northwest. Thus, the net suspended sediment flux over the entire tidal cycle was directed towards the northwest, with a magnitude of 10^2 kg m^{-1} .

For the middle intertidal flat, i.e. at Station M03, the lateral components were similar to or larger than the longitudinal ones (Table 4). However, at Station M08, the lateral fluxes were lower than the longitudinal ones in all but one case. Lateral transport was towards the west (land) and the net sediment transport was landwards at M08 in May 2008. However, the net fluxes were directed offshore due to the presence of an adjacent southeastward tidal creek (connecting with the Wanggang River and affected by the artificially-controlled river discharges during ebb) at M03 in July 2003. Thus, localized geomorphological features can significantly affect the net sediment transport. In addition, although the suspended sediment transport rate increases in response to enhanced current velocities and SSCs during flood or ebb, the net suspended sediment flux during the tidal cycle may not increase significantly, e.g. at Station M03 on July 4, 2003 (Table 4). As far as the observations of relatively large net fluxes on July 3–4 and 5 (2003), this pattern may be explained by the fact that prolonged seaward currents, strong winds and heavy rainfall caused by the rainstorm event enhanced the seaward sediment transport and the asymmetry of the flood-ebb transport capacity (or phase), which was superimposed onto the influence of the ebb-dominated tidal creek.

At Stations S1 and S3 over the lower tidal flat, lying close to MLWL, the suspended sediment fluxes were dominated by the longitudinal component, which was several times greater than the lateral component. Nevertheless, the lateral landward fluxes here are similar to the corresponding ones over the middle intertidal flat (e.g. at Station M08). This pattern would ensure sufficient sediment supply to enhance the onshore accretion of the intertidal flat. The large longitudinal component is caused by the strong tidally-induced longshore currents.

The measurements at C06 (on May 14–16, 2006) in a tidal creek show that the creek is characterized by rectilinear currents. Since the tidal creek is located in the salt marsh, the current velocities were weak, i.e. a maximum velocity of less than 0.2 m s^{-1} , which was insufficient to entrain the local bottom sediment. However, the SSC reached up to 1900 mg L^{-1} due to the advective transport from nearby intertidal flats. The suspended sediment fluxes were 15.45 kg m^{-1} and 14.51 kg m^{-1} during the flood period on July 15 and 16, 2006, respectively. These fluxes were much higher than the fluxes of 2.06 kg m^{-1} and 2.60 kg m^{-1} during the ebb tide period. Thus, the net sediment transport was directed into the tidal creek, which was consistent with accretion occurring around the creek levees whose elevations were higher than that of the adjacent salt marshes.

4.5. Short-term changes in surface sediment and bed morphology

Leveling measurements show that the elevation of the profile P1 experienced significant accretion from May to December, 2008 (Fig. 9). The maximum and minimum accretion thicknesses were 0.63 m over the lower intertidal flat and 0.18 m at upper intertidal flat, respectively. This pattern implies that the rate of sediment accumulation ranged between 0.80 mm and 2.82 mm per day. The mean slope of the intertidal flat was 0.091% between the 2008 seawall and Station S3,

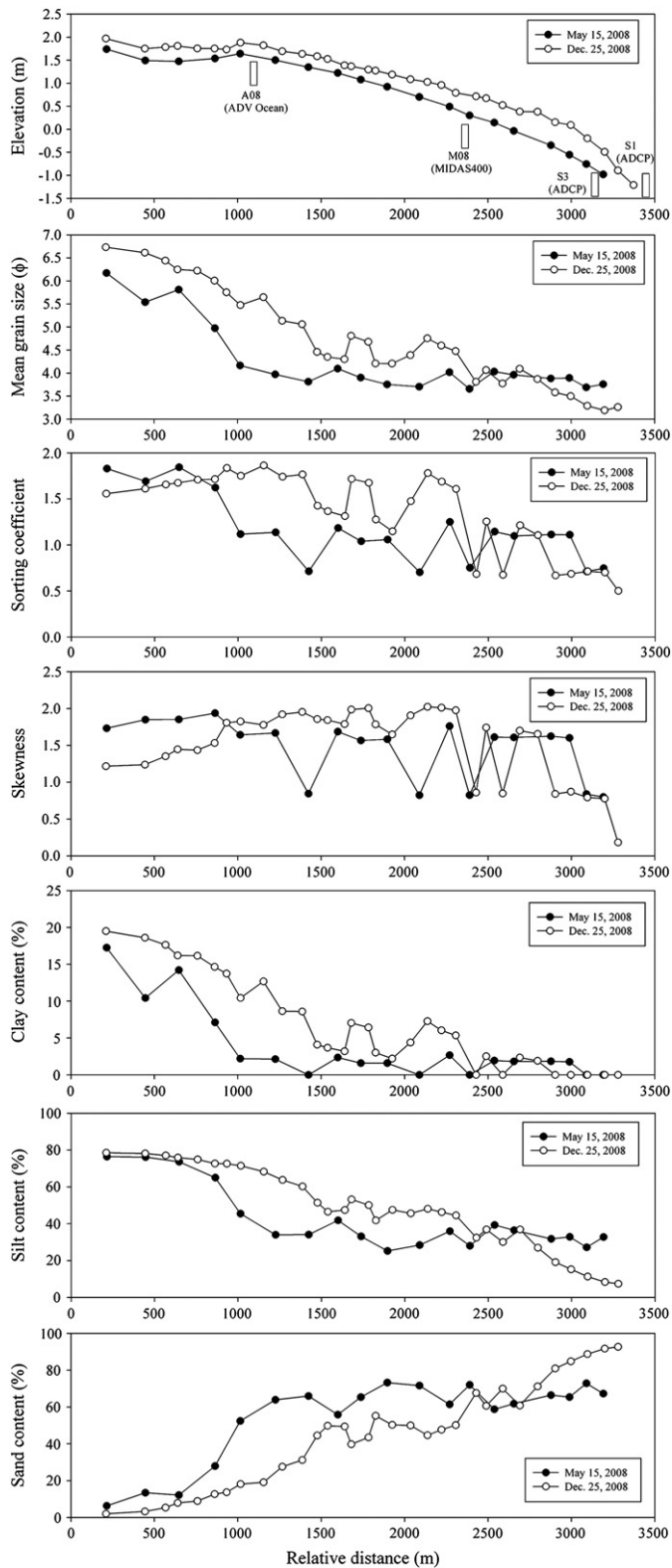


Fig. 9. Seabed elevation changes along profile P1 (for location, see Fig. 1C) and corresponding grain size parameter variations from May to December, 2008. The relative distance begins from the 2008 seawall.

measured in May, which decreased to 0.082% in December. This change could be an adjustment of the intertidal flat to reclamation and the construction of the seawall in 2008.

In general, the grain size of the seabed sediment coarsens seawards, ranging from 6.2–6.7 ϕ to 3.2–3.6 ϕ (Fig. 9). Sorting was improving

seaward, with skewness much closer to a normal distribution over the lower intertidal flat. In addition, the clay and silt content increased significantly over the mid-upper intertidal flats, respectively. On the lower intertidal flat, the silt content decreased to 7.4% and the sand content increased significantly, to 92.6%.

The surficial sediments did not contain any clay on the lower tidal flat (e.g. a relative distance of 2400 m seaward on Fig. 9). However, the suspended sediment contained clay contents in excess of 13% during the flood (Fig. 8). This clay is considered to have been supplied by the adjacent sea, i.e. the offshore sandbanks (with clay contents of up to 18% in the north and southeast sandbank areas, surveyed by authors in 2006–2007) and from coastal erosion. Thus, the clay sediment transported to the mid-upper intertidal flat is supplied from extraneous sources rather than local resuspension.

Grain size trend analysis suggests that sediment was transported offshore near the seawall but landwards from the mid-lower intertidal flats in May, 2008 (Fig. 10). The sediment convergence area is a high levee at a relative distance of 1000 m, which is geomorphological evidence for accretion. Within the region lying from the levee to the seawall, an accretional area was present with muddy and cohesive sediment; the slope was much more gentle here, i.e. 0.012%. From the levee to the sea, the surficial sediment of the intertidal flat consists of non-cohesive silt and sand. The slope was increased to 0.12% here which was ten times of that of the upper flat.

However, the muddy and cohesive sediment extended seaward to the relative distance of 2000 m in December, 2008 (Fig. 9). The sediment transport pattern became complex, although the entire area was accretional. The sediment convergence area was still present at a relative distance of 1000 m from the 2008 seawall. Nevertheless, the sediment was transported landwards near the seawall. Over the lower intertidal flat, the sediment was transported seawards which trended to reduce the slope of intertidal flat. The leveling undertaken shows that the slope of this profile decreased from 0.12% in May to 0.10% in December, 2008.

5. Discussion

The results outlined above show that the intertidal flat is controlled by multiple frequencies of dynamic forcing and environmental conditions, including winds, locally-generated wind waves, tides and tidal currents, storm events, river discharges, and the local morphological features (e.g. tidal creeks, levees and varying bed slopes). These general patterns are similarly observed over other intertidal flats, on a worldwide basis. However, there are still some site-specific characteristics of the study area, which is characterized by highly turbid waters and a monsoon climate; superimposed with sequential reclamation, an intense human activity of the region. The wind speeds and directions measured at Dafeng Harbor in 2007 show a seasonal variation controlled by the East Asian monsoon. SE and SSE winds dominate in spring, representing 28% of the total, with a mean speed of 3.7 m s^{-1} and a maximum speed of 15.0 m s^{-1} (Fig. 11). However, the NW, NNW, WNW and W winds accounted for 64% and 58% of the total, in summer and winter, respectively. The corresponding maximum wind speeds were 9.6 m s^{-1} , and 11.9 m s^{-1} . The autumn was dominated by northerly winds (15.8%), with a maximum wind speed of 11.8 m s^{-1} (Fig. 11). Dafeng intertidal flat is sheltered by the south and east offshore sand ridges, and only the wind from the north has a large fetch in autumn. This is confirmed by the observed high SSC in the adjoining sea (Xing, 2010). During other seasons, the fetch is limited, which is similar to the situation of the Ho Bugt tidal flat in the Wadden Sea (Christiansen et al., 2006); however, it is very different from the estuarine tidal flat open to the sea with a direct and stronger wave influence (e.g. Osborne and Vincent, 1996; Fan et al., 2002).

The strong wind and long fetch could cause erosion in autumn on the wide intertidal flat, which was surveyed previously by Yang (1982) and Ren et al. (1983) who observed “mud boulders” and “mud

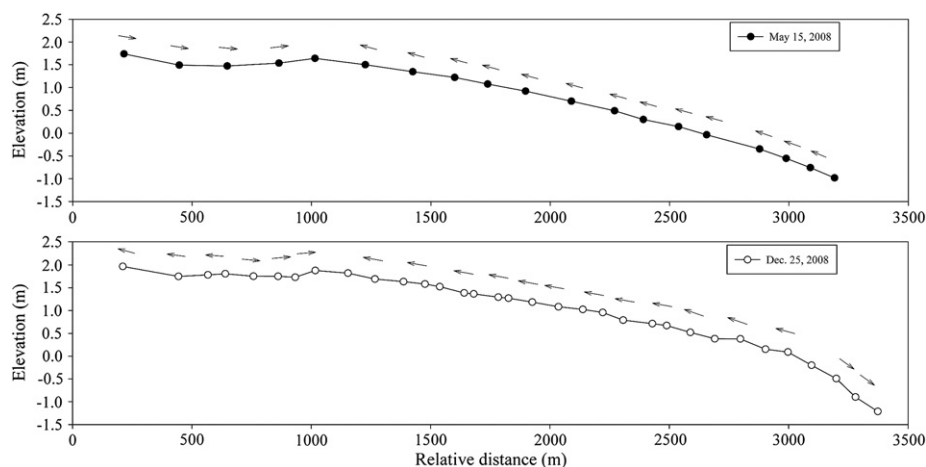


Fig. 10. Net sediment transport patterns crossing the intertidal flat (P1 profile), as derived from the grain size trend analysis.

bastions" on the surface of the Dafeng intertidal flat in October. However, these seasonal scouring features have disappeared during recent years according to our observations. Comparison of leveling data, between May and December (2008), reveals siltation patterns over the intertidal flat, which are likely associated with the reclamation activities which have induced a significant decrease of the tidal prism, and in a way, weakened tidal currents over the upper and middle tidal flat, resulting in rapid accumulation. The seabed friction and dissipation are significant in relation to a combined current and wave motion in the shallow sea, as observed elsewhere (Christoffersen and Jonsson, 1985). The wave measurements along the P1 profile in 2008 show that the significant wave height and energy density attenuates with rates of 0.024–0.032% and 0.041–0.051% per meter landward, respectively (Qin et al., 2010). The

maximum width of the tidal flat was more than 15 km before 1978 (Yang, 1982), whilst the width was 7–10 km before the reclamation in 2000. Hence, significant dissipation of wave energy took place over the intertidal flat before the reclamations. The reduction in the intertidal flat width would cause a concentration of wave energy on the lower intertidal flat and in the sub-tidal areas, with relative deep water, resulting in higher SSC than recorded in the historical data (Fig. 12).

The hydrodynamics become stronger towards the sea across the intertidal flat, with the maximum current velocity of 0.47 m s^{-1} on the upper and 1.41 m s^{-1} on the lower intertidal flat, with the strength of the longitudinal components of the current increasing with distance towards the sea on May 9, 2008 (Fig. 12). However, the residual current is stronger landward on the mid-upper intertidal flats than on

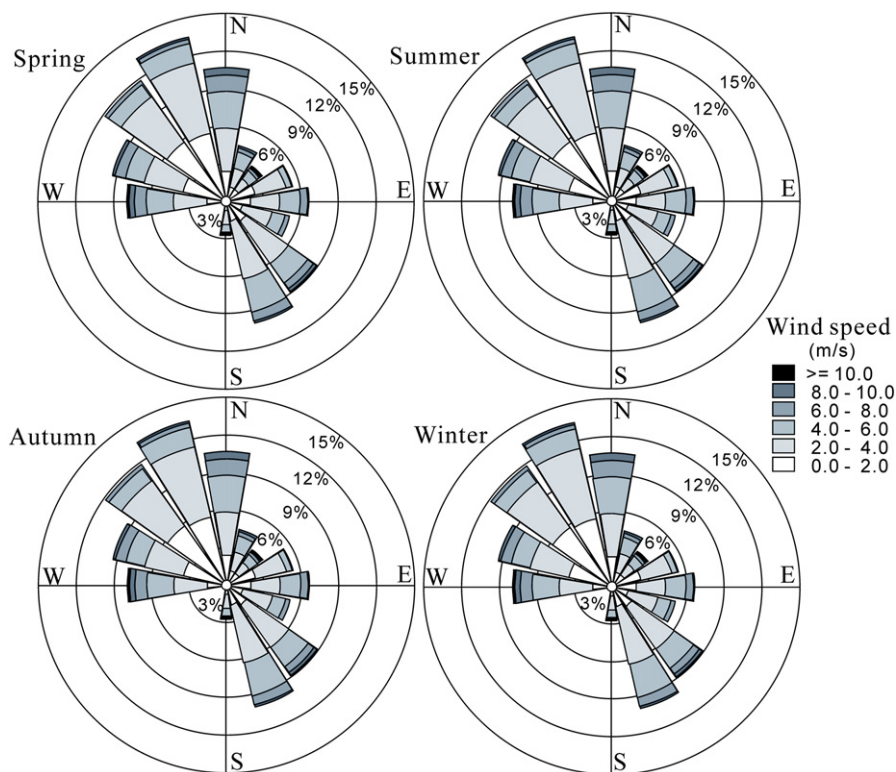
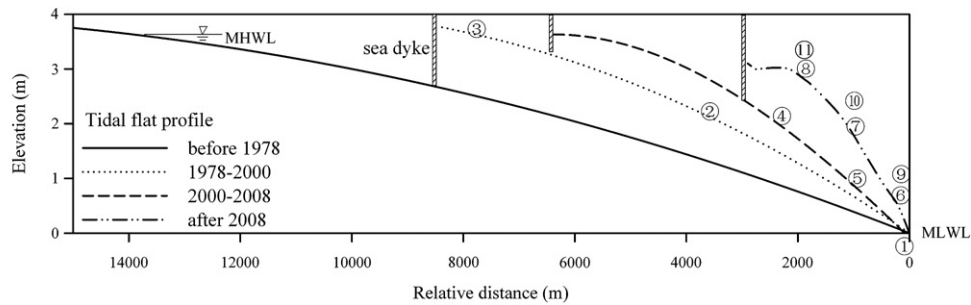


Fig. 11. Rose diagrams showing wind directions and speeds, measured at Dafeng Harbor.



Location	Measurement date	Max. depth-averaged current speed (m/s)		SSC(mg/L)		Seabed median grain size(Φ)
		Flood	Ebb	Flood	Ebb	
①	1980/9/13	0.92	0.76	3070	2000	3.9
②		0.5	0.44	1840	1440	4.3
③		0.52	0.38	1160	1060	5.56
④	2000/10/16	0.49	0.74	2610	3690	4.56
⑤	2003/7/3	0.34	0.63	1370	1466	3.64
⑥		1.41	0.71	4906	5938	3.53
⑦	2008/5/9	0.37	0.58	1489	1484	3.6
⑧		0.47	0.28	1942.8	1629.5	3.8
⑨	2008/12/15					3.31
⑩						3.74
⑪						5.1

Fig. 12. Sketch map of the Dafeng intertidal flat profiles, showing sediment dynamic parameters associated with historical morphological changes.

the lower intertidal flat (cf. Table 4), which may be due to the wave and tide deformation in the shallow waters (Dronkers, 1986). Under such conditions, suspended sediment transport should be directed landward over the intertidal flat. In addition, abundant suspended sediments are supplied from the adjoining sea, e.g. the offshore sand ridge areas (Ren et al., 1983), which is transported by advection during the flood period; thus, sometimes the relationship between SSCs and the current velocities is insignificant over the intertidal flat. Furthermore, the current is flood-dominated on the lower tidal flat close to MLWL (e.g. ① and ⑥ in Fig. 12). Hence, the lateral component of the current velocity controls the quantity of the onshore suspended sediment flux. The strong flood current measured at the lower tidal flat in 2008, with a maximum depth-averaged current speed of 1.41 ms^{-1} , could result in intense sediment transport and accretion over the tidal flat. The evidence is such that the deposition rate measured in 2008 reached up to 1.86 mm day^{-1} . Previous study in this area shows that the deposition rates, on the basis of the ^{210}Pb dating, were about $10\text{--}30 \text{ mm yr}^{-1}$ (Ke, 1999) and $31\text{--}33 \text{ mm yr}^{-1}$ (Wang et al., 2005). Further study is required on the long-time monitoring of the seabed elevation changes.

On such an accretional intertidal flat, sedimentation patterns are related to local bed geomorphology. Previous studies have shown that accretion-dominated intertidal flats tend to be highly convex in cross-sectional shape (Kirby, 2000; Roberts et al., 2000). Hence, the slope of the middle intertidal flat is relatively high. Since the current speed is inversely proportional to the local bed slope (Wang et al., 1999), a low current speed (onshore-offshore component) might be expected over the steep area, which will in turn enhance the deposition and accretion. Thus, the intertidal flat becomes more convex. In the case of the Dafeng intertidal flat, this occurred in the periods before 1980, when the intertidal flat was influenced mainly by natural conditions. However, human activities (i.e. reclamation) had interrupted this process. Fig. 12 shows that the maximum depth-averaged current speed observed over the middle intertidal flat was similar to those over the upper intertidal flat, being almost symmetrical between the flood and ebb in 1980. However, a strong tidal asymmetry was present over the middle intertidal flat, with a stronger current speed during the ebb than that during the flood after 2000. This promoted a

negative feedback such that the ebb current could transport sediment offshore and lessen the seabed slope over the middle intertidal flat, which would be expected to be steeper under natural conditions. Over the newly reclaimed tidal flat in the early 2008, the grain size of surficial sediment close to the sea dyke (⑧ in Fig. 12) was not significantly affected by the reclamation and still coarser in May, 2008 (3.8Φ) than the same site (④ in Fig. 12) in October (4.56Φ), 2000. However, the grain size of the seabed sediment showed a response to the accretion (cf. Fig. 9), becoming finer following the reclamation, from 3.8 in May to 5.1 in December, 2008 (Fig. 12). The survey also showed that the mud area (with soft and cohesive surficial sediment) extended from the upper tidal flat in May to the middle tidal flat in December, 2008. This observation is consistent with model output that the mud zone would extend towards the sea if sediment supply is abundant and the intertidal flat has a small width (Gao, 2009a).

Because the sediment supply to the narrowed intertidal area following reclamation was maintained, rapid siltation continued. The convex shape of the cross-section was roughly maintained (Fig. 9), although the waves appeared somewhat intense over the intertidal flat, in comparison with intertidal flats elsewhere (e.g. Garolim Bay, Korea (Lee et al., 2004)). A conceptual model established by Kirby (2000) has shown that imposed strong waves over an intertidal flat could convert a high and convex cross-sectional shape, into a low and concave profile. However, the concave shape of the upper part of the intertidal flat, close to the seawall (Figs. 9 and 10), is not the case here. The slope of the intertidal flat would become steeper in response to rapid and sequential reclamation, to form a high levee on the mid-upper intertidal flat (i.e. at the location of 1000 m, in Fig. 9); this decreased significantly the inundation time of this area, during neap-spring tidal cycles. Thus, the deposition would be limited to the upper part between the levee and seawall. On the other hand, the MLWL did not significantly extend seaward following reclamations; this has been indicated by the survey and Landsat TM images over the last decade (Wang and Zou, 2009). The bathymetry of sub-tidal area almost maintained from 1979 to 2006 (Fig. 1B, C). A model applied to the accreting intertidal flat on the central Jiangsu coast shows that intertidal flats with abundant sediment supply can persistently prograde with the similar slope, remaining in the equilibrium shape

under natural conditions (Liu et al., 2010). However, such an equilibrium shape with similar slope cannot be maintained for the study area under the influence of rapid reclamations. The intertidal area has become progressively steeper and narrower (Fig. 12).

6. Conclusions

Analysis of the data sets obtained from an accretional intertidal flat along the Jiangsu coast, affected by intense reclamation reveals that due to the shoaling effect and the influence of an artificial sea wall, the tidal wave becomes irregular over the intertidal flat; this, in further, modifies the time–velocity asymmetry patterns over the intertidal flat. Northerly winds in autumn used to cause erosion, but this seasonal scouring disappeared following the sequential reclamation in 2000.

Over the lower intertidal flat, the residual currents were observed to be directed landward in the upper layer of the water column but seaward in the lower layer. The grain size of suspended sediment was finer in the upper layer than in the bottom layer. Furthermore, the suspended sediment is finer, with a higher clay content, during the flood than during the ebb. These patterns lead to the transport of fine-grained sediment onshore, together with coarse sediment offshore.

On this particular intertidal flat, suspended sediment fluxes are dominated by the longshore component near to MLWL, which is several times larger than the onshore-offshore component. Nevertheless, the onshore-offshore fluxes provide sufficient sediment supply for the accretion of the intertidal flat. Near tidal creeks (or channels), net suspended sediment transport is affected strongly by the creek characteristics and associated hydrodynamics. The continuous accumulation of sediment, following reclamation, implies that the equilibrium shape of the intertidal flat cross-section under natural conditions cannot be maintained under the influence of rapid reclamations, with the mud zone extending seaward and occupying the former sand flat. Thus, the shape of tidal flat is composed two parts: a concave upper part with gentle slope and a convex mid-lower part with steep slope.

Acknowledgements

Financial support to the study was provided by the National Natural Science Foundation of China (grant nos. 40876043 and 40576040). The authors wish to thank Li ZH, Wang AJ, Du XQ, Zuo H, Xing F, Li JS, Liu YL, Cheng J, Wang HQ, Ran Q and Zhu JQ who participated in the field work, and Chen YN and Li J for her help in grain size analysis. Prof. Collins MB, Prof. Li Y and Dr. Chen YN are thanked for their comments on an early version of the text. The reviewers are thanked for their critical and constructive comments on the original manuscript.

References

- Allen, J.R.L., 2000. Morphodynamics of Holocene salt marshes: a review sketch from the Atlantic and Southern North Sea coasts of Europe. *Quaternary Science Reviews* 19, 1155–1231.
- Allen, J.R.L., Pye, K., 1992. Coastal saltmarshes: their nature and importance. In: Allen, J.R.L., Pye, K. (Eds.), *Saltmarshes, Morphodynamics, Conservation and Engineering Significance*. Cambridge University Press, Cambridge, U.K, pp. 1–18.
- Andersen, T.J., Pejrup, M., Nielsen, A.A., 2006. Long-term and high-resolution measurements of bed level changes in a temperate, microtidal coastal lagoon. *Marine Geology* 226, 115–125.
- Christiansen, C., Volund, G., Lund-Hansen, L.C., Bartholdy, J., 2006. Wind influence on tidal flat sediment dynamics: field investigations in the Ho Bugt, Danish Wadden Sea. *Marine Geology* 235, 75–86.
- Christie, M.C., Dyer, K.R., Turner, P., 1999. Sediment flux and bed level measurements from a macro tidal mudflat. *Estuarine, Coastal and Shelf Science* 49, 667–688.
- Christoffersen, J.B., Jonsson, I.G., 1985. Bed friction and dissipation in a combined current and wave motion. *Ocean Engineering* 12, 387–423.
- Chung, C.H., Zhuo, R.Z., Xu, G.W., 2004. Creation of *Spartina* plantations for reclaiming Dongtai, China, tidal flats and offshore sands. *Ecological Engineering* 23, 135–150.
- Collins, M.B., Ke, X., Gao, S., 1998. Tidally-induced flow structure over intertidal flats. *Estuarine, Coastal and Shelf Science* 46, 233–250.
- de Haas, H., Eisma, D., 1993. Suspended-sediment transport in the Dollard estuary. *Netherlands Journal of Sea Research* 31, 37–42.
- Dronkers, J., 1986. Tidal asymmetry and estuarine morphology. *Netherlands Journal of Sea Research* 20, 117–131.
- Dyer, K.R., 2000. Preface (properties of intertidal mudflats). *Continental Shelf Research* 20, 1037–1038.
- Fan, D., Li, C., Archer, A.W., Wang, P., 2002. Temporal distribution of diastems in deposits of an open-coast tidal flat with high suspended sediment concentrations. *Sedimentary Geology* 152, 173–181.
- French, C.E., French, J.R., Clifford, N.J., Watson, C.J., 2000. Sedimentation–erosion dynamics of abandoned reclamations: the role of waves and tides. *Continental Shelf Research* 20, 1711–1733.
- Gao, S., 1996. A Fortran program for grain-size trend analysis to define net sediment transport pathways. *Computers and Geosciences* 22, 449–452.
- Gao, S., 2009a. Modeling the preservation potential of tidal flat sedimentary records, Jiangsu coast, eastern China. *Continental Shelf Research* 29, 1927–1936.
- Gao, S., 2009b. Geomorphology and sedimentology of tidal flats. In: Perillo, G.M.E., Wolanski, E., Cahoon, D., Brinson, M. (Eds.), *Coastal Wetlands: An Ecosystem Integrated Approach*. Elsevier, Amsterdam, pp. 295–316.
- Gao, S., Collins, M.B., 1992. Net sediment transport patterns inferred from grain-size trends, based upon definition of “transport vectors”. *Sedimentary Geology* 81, 47–60.
- Green, M.O., Coco, G., 2007. Sediment transport on an estuarine intertidal flat: measurements and conceptual model of waves, rainfall and exchanges with a tidal creek. *Estuarine, Coastal and Shelf Science* 72, 553–569.
- Green, M.O., Black, K.P., Amos, C.L., 1997. Control of estuarine sediment dynamics by interactions between currents and waves at several scales. *Marine Geology* 144, 97–116.
- Hequette, A., Aernouts, D., 2010. The influence of nearshore sand bank dynamics on shoreline evolution in a macrotidal coastal environment, Calais, Northern France. *Continental Shelf Research* 30, 1349–1361.
- JCC (Jiangsu Chorography Committee), 1995. *Chorography of Jiangsu Province: Tidal Flat Exploitation*. Jiangsu Science and Technology Press, Nanjing. (in Chinese).
- Jia, J., Wang, Y., Gao, S., Wang, A., Li, Z., 2006. Interpreting grain-size trends associated with bedload transport on the intertidal flats at Dafeng, central Jiangsu coast. *Chinese Science Bulletin* 51, 341–351.
- Johns, B., 1983. *Physical Oceanography of Coastal and Shelf Seas*. Elsevier Publisher, Amsterdam.
- Ke, X., 1999. Report for the Tidal Flat Reclamation at the South of Dafeng Harbor, Jiangsu. (in Chinese).
- Kirby, R., 2000. Practical implications of tidal flat shape. *Continental Shelf Research* 20, 1061–1077.
- Kremer, H.H., Le Tissier, M.D.A., Burbridge, P.R., Talaue-McManus, L., Rabalais, N.N., Parslow, J., Crossland, C.J., Young, B., 2005. IGBP Report 51 / IHDP Report 18. *Land–Ocean Interactions in the Coastal Zone (LOICZ): Science Plan and Implementation Strategy Structure*.
- Le Hir, P., Roberts, W., Cazaillet, O., Christie, M., Bassoullet, P., Bacher, C., 2000. Characterization of intertidal flat hydrodynamics. *Continental Shelf Research* 20, 1433–1459.
- Lee, H.J., Jo, H.R., Chu, Y.S., Bahk, K.S., 2004. Sediment transport on macrotidal flats in Garolim Bay, west coast of Korea: significance of wind waves and asymmetry of tidal currents. *Continental Shelf Research* 24, 821–832.
- Leffler, K.E., Jay, D.A., 2009. Enhancing tidal harmonic analysis: Robust (hybrid $L1 = L2$) solutions. *Continental Shelf Research* 29, 78–88.
- Liu, Z., Huang, Y., Zhang, Q., 1989. Tidal current ridges on the southwestern Yellow Sea. *Journal of Sedimentary Petrology* 59, 432–437.
- Liu, X.J., Gao, S., Wang, Y.P., 2010. Modeling cross-sectional shape evolution for accreting tidal flat: a case study of the central Jiangsu coast. unpublished manuscript.
- Mai, S., Bartholomä, A., 2000. The missing mud flats of the Wadden Sea: a reconstruction of sediments and accommodation space lost in the wake of land reclamation. *Proceedings in Marine Science* 2, 257–272.
- McManus, J., 1988. Grain size determination and interpretation. In: Tucker, M. (Ed.), *Techniques in Sedimentology*. Backwell, Oxford, pp. 63–85.
- Osborne, P.D., Vincent, C.E., 1996. Vertical and horizontal structure is suspended sand concentrations and wave-induced fluxes over bedforms. *Marine Geology* 131, 195–208.
- Pritchard, D., Hogg, A.J., 2003. Cross-shore sediment transport and the equilibrium morphology of mudflats under tidal currents. *Journal of Geophysical Research* 108, 2003–3313.
- Qin, Q., Wang, Y.P., Gao, J., Yang, Y., 2010. Wave attenuation over the Wanggang intertidal flat, Jiangsu. Unpublished manuscript.
- Quaresma, V.D.S., Bastos, A.C., Amos, C.L., 2007. Sedimentary processes over an intertidal flat: a field investigation at Hythe flats, Southampton Water (UK). *Marine Geology* 241, 117–136.
- Ren, M.E., 1986. Tidal mud flat. In: Ren, M.E. (Ed.), *Modern Sedimentation in the Coastal and Nearshore Zones of China*. China Ocean Press, Beijing, pp. 78–127.
- Ren, M.E., Zhang, R., Yang, J., 1983. Sedimentation on tidal mud flat of Wangang area, Jiangsu Province, China. *Collected Oceanic Works* 6, 84–108.
- Roberts, W., Le Hir, P., Whitehouse, R.J.S., 2000. Investigation using simple mathematical models of the effect of tidal currents and waves on the profile shape of intertidal mudflats. *Continental Shelf Research* 20, 1079–1097.
- Ryan, N.M., Cooper, J.A.G., 1998. Spatial variability of tidal-flats in response to wave exposure: examples from Strangford Lough, Northern Ireland. In: Black, K.S., Paterson, D.M., Cramp, A. (Eds.), *Sedimentary Processes in the Intertidal Zone: Geological Society of London, Special Publication*, 139, pp. 221–230.
- Soulsby, R.L., 1997. *Dynamics of Marine Sands: A Manual for Practical Applications*. Thomas Telford Publications, London.

- Symonds, A.M., Collins, M.B., 2007. The establishment and degeneration of a temporary creek system in response to managed coastal realignment: the Wash, UK. *Earth Surface Processes and Landforms* 32, 1783–1796.
- van Rijn, L.C., 1993. *Principles of Sediment Transport in Rivers, Estuaries and Coastal Seas*. Aqua Publications, Amsterdam, the Netherlands.
- Wang, Y. (Ed.), 2002. *Radiative Sandy Ridge Field on Continental Shelf of the Yellow Sea*. China Environment Science Press, Beijing (in Chinese).
- Wang, X., Ke, X., 1997. Grain-size characteristics of the extant tidal flat sediments along the Jiangsu coast, China. *Sedimentary Geology* 112, 105–122.
- Wang, Y., Zou, X., 2009. A report on the exploitation feasibility of an 10,000-ton harbor in Dafeng. Nanjing University. (in Chinese).
- Wang, Y.P., Zhang, R., Gao, S., 1999. Velocity variations in salt marsh creeks, Jiangsu, China. *Journal of Coastal Research* 15, 471–477.
- Wang, Y., Gao, S., Ke, X., 2004. Measurements of boundary layer parameters and suspended sediment transport over the intertidal flats of northern Jiangsu, China. *Acta Oceanologica Sinica* 23, 437–448.
- Wang, A., Gao, S., Jia, J., Pan, S., 2005. Sedimentation rates in the Wanggang salt marshes, Jiangsu. *Journal of Geographical Sciences* 15, 199–209.
- Wang, Y., Gao, S., Jia, J., 2006. High-resolution data collection for analysis of sediment dynamic processes associated with combined current-wave action over intertidal flats. *Chinese Science Bulletin* 51, 866–877.
- Widdows, J., Brinsley, M.D., Salkeld, P.N., Lucas, C.H., 2000. Influence of biota on spatial and temporal variation in sediment erodability and material flux on a tidal flat (Westerschelde, The Netherlands). *Marine Ecology Progress Series* 194, 23–37.
- Xing, F., 2010. Hydrodynamics and suspended sediment transport in the vicinity of radial sand ridges, southern Yellow Sea. M.Sc. thesis, Nanjing University.
- Yang, J.H., 1982. Sedimentation on intertidal mudflats near Wanggang of Dafeng, Jiangsu Province. M.Sc. Thesis, Nanjing University, China (in Chinese).
- Yang, S., Chen, J., 1995. Coastal salt marshes and mangrove swamps in China. *Chinese Journal of Oceanology and Limnology* 13, 318–324.
- Yang, Y., Wang, Y.P., Gao, S., 2003. Hydrodynamic processes and suspended sediment transport in the salt-marsh creeks, Wanggang, Jiangsu (in Chinese with an English abstract). *Marine Geology & Quaternary Geology* 23, 23–28.
- Zhang, R., 1992. Suspended sediment transport processes on tidal mud flat in Jiangsu Province, China. *Estuarine, Coastal and Shelf Science* 35, 225–233.
- Zhou, H.X., Liu, J.E., Zhou, J., Qin, P., 2008. Effect of an alien species *Spartina alterniflora* Loisel on biogeochemical processes of intertidal ecosystem in the Jiangsu coastal region, China. *Pedosphere* 18, 77–85.